

This is the accepted manuscript made available via CHORUS. The article has been published as:

Doping-dependent correlation effects in
 $(\text{Sr}_{1-x}\text{La}_x)_3\text{Ir}_2\text{O}_7$

Gregory Affeldt, Tom Hogan, Jonathan D. Denlinger, Ashvin Vishwanath, Stephen D. Wilson, and Alessandra Lanzara

Phys. Rev. B **97**, 125111 — Published 9 March 2018

DOI: [10.1103/PhysRevB.97.125111](https://doi.org/10.1103/PhysRevB.97.125111)

Doping dependent correlation effects in $(\text{Sr}_{1-x}\text{La}_x)_3\text{Ir}_2\text{O}_7$

Gregory Affeldt,^{1,2} Tom Hogan,^{3,4} Jonathan D. Denlinger,⁵ Ashvin Vishwanath,^{1,2} Stephen D. Wilson,⁶ and Alessandra Lanzara^{1,2}

¹*Materials Sciences Division, Lawrence Berkeley National Laboratory, Berkeley, CA*

²*Department of Physics, University of California, Berkeley, CA*

³*Department of Physics, Boston College, MA*

⁴*Materials Department, University of California, Santa Barbara, CA*

⁵*Advanced Light Source, Lawrence Berkeley National Laboratory, Berkeley, CA*

⁶*Materials Department, University of California Santa Barbara, Santa Barbara, CA*

(Dated: February 7, 2018)

Abstract

We have measured the signatures of electronic energy scales and their doping evolution in the band structure of $(\text{Sr}_{1-x}\text{La}_x)_3\text{Ir}_2\text{O}_7$ using angle-resolved photoemission spectroscopy (ARPES). While band splittings and positions corresponding to the bilayer splitting and spin-orbit coupling undergo only small changes, the Mott gap and effective mass of both the lower Hubbard band and conduction band exhibit strong variations with doping. These changes correspond to similar observations in the cuprate superconductors, and are likely connected to the changing effective Coulomb interaction upon addition of itinerant carriers.

1 Much recent progress has been made in understanding the nature of the spin-orbit Mott
 2 state in the layered perovskite iridates^{2,3,6,12-14,16-18,24,27-29,32,36}, in which spin-orbit coupling
 3 and Coulomb electron-electron correlations combine to form an insulating state. The spin-
 4 orbit coupling arranges the t_{2g} bands by an effective angular momentum into a filled $J_{\text{eff}} = \frac{3}{2}$
 5 state and a half-filled $J_{\text{eff}} = \frac{1}{2}$ state. The Coulomb correlation is sufficient to localize the
 6 $J_{\text{eff}} = \frac{1}{2}$ electrons in a Mott state, with Mott-like gaps observed in both the single-layer
 7 Sr_2IrO_4 ¹³ and the the bilayer $\text{Sr}_3\text{Ir}_2\text{O}_7$ ^{24,32}. When the former is doped with electrons, either
 8 via La substitution on the Sr site³¹ or via the surface deposition of potassium atoms¹⁷, band
 9 structures highly similar to the cuprates emerge with Fermi arcs, pseudogaps, and evidence
 10 of a d -wave gap that may be indicative of superconductivity in the case of the potassium
 11 surface doping^{16,34}. Hole-doping in $\text{Sr}_2\text{Ir}_{1-x}\text{Rh}_x\text{O}_4$ is also reported to establish Fermi arc
 12 and pseudogap states, though with a markedly different Fermi surface⁴. These and other
 13 related observations have lent additional credence to the notion that pseudogap phases arise
 14 essentially from the physics of a doped Mott insulator.

15 Bilayer $\text{Sr}_3\text{Ir}_2\text{O}_7$ exhibits several important differences from the single layer Sr_2IrO_4 . In
 16 addition to its larger bandwidth and smaller Mott gap, the magnetic moments in the anti-
 17 ferromagnetic state in $\text{Sr}_3\text{Ir}_2\text{O}_7$ align along the crystallographic c -axis³ (rather than in the
 18 ab plane as in Sr_2IrO_4 ¹⁵ and the cuprates), and the magnetic excitation spectrum exhibits
 19 a large magnon gap¹⁴. Upon doping in $(\text{Sr}_{1-x}\text{La}_x)_3\text{Ir}_2\text{O}_7$, the parent antiferromagnetic in-
 20 sulating state gives way to a paramagnetic metallic state near $x = 4\%$ ^{12,19} with short-range
 21 antiferromagnetic correlations persisting out to at least $x = 6.5\%$ ²². No signatures of super-
 22 conductivity have been reported in this system. Additionally, it exhibits small electron-like
 23 Fermi surface pockets and a low-energy suppression of spectral weight in the antiferromag-
 24 netic state¹ instead of the large hole-like Fermi surface with anisotropic pseudogap and Fermi
 25 arcs in Sr_2IrO_4 . A recent ultrafast reflectivity study has also revealed a charge density-wave
 26 like instability in the metallic regime⁷ that may be connected to a structural distortion ob-
 27 served via x-ray scattering, suggesting that charge-lattice interactions also play an important
 28 role in $(\text{Sr}_{1-x}\text{La}_x)_3\text{Ir}_2\text{O}_7$ ¹².

29 Here we present a doping-dependent study of the electronic structure of electron-doped
 30 $(\text{Sr}_{1-x}\text{La}_x)_3\text{Ir}_2\text{O}_7$ ($0.01 \leq x \leq 0.06$) using angle-resolved photoemission spectroscopy
 31 (ARPES). As doping increases, the Mott gap decreases and an electron-like conduction
 32 band appears near the M point. These changes are accompanied by a shift of the band

33 structure beyond a simple rigid-shift picture of doping, including an increase of the effective
 34 mass of both the conduction band and lower Hubbard band. In contrast, band splittings
 35 related to both the bilayer interaction and spin-orbit coupling are nearly constant with
 36 doping. These results mirror previous observations in the cuprates and other transition
 37 metal oxides near the Mott state, suggesting a similar role of Mott physics in this system.

38 Single-crystal samples of $(\text{Sr}_{1-x}\text{La}_x)_3\text{Ir}_2\text{O}_7$ were synthesized using a flux method as de-
 39 scribed elsewhere¹². ARPES measurements were performed at beamlines 4.0.3 and 10.0.1
 40 of the Advanced Light Source at temperatures ranging from 15 K to 240 K. The samples
 41 were cleaved *in situ* and measured at pressures better than 6×10^{-11} Torr. The chemical
 42 potential was referenced to a polycrystalline gold surface evaporated *in situ* on the sample
 43 puck for measurements at beamline 4.0.3 or a separate calibrating gold film sample with
 44 identical beamline configuration at ALS beamline 10.0.1.

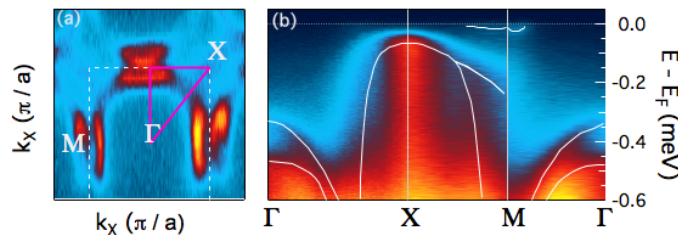


FIG. 1. Fermi surface and dispersion in $(\text{Sr}_{0.94}\text{La}_{0.06})_3\text{Ir}_2\text{O}_7$. (a): Fermi surface of the $x = 6\%$ sample. The white dashed square is the boundary of the reduced BZ. (b): Energy-momentum distribution of ARPES intensity along high symmetry directions in the first Brillouin zone. White curves are guides to the eye for the band dispersions.

45 The experimental ARPES signatures of electronic correlations studied in this paper are
 46 illustrated in figure 1 for a metallic $(\text{Sr}_{0.94}\text{La}_{0.06})_3\text{Ir}_2\text{O}_7$ ($x = 6\%$) sample. The low-energy
 47 dispersion is seen in the energy-momentum cut in figure 1(b) along high symmetry directions
 48 in the first Brillouin zone. White curves are guides to the eye for the dispersion of the four
 49 bands visible in this energy window. The small electron-like bands near the M point give rise
 50 to the lens-shaped Fermi surface seen in figure 1 (a). LDA+SOC+U calculations show the
 51 minimum of the upper Hubbard band near the M point, but whether the band observed in
 52 ARPES is the upper Hubbard band or an in-gap state remains to be conclusively determined.
 53 Since in the more heavily doped samples this band crosses the Fermi level, we follow previous

54 ARPES works^{9,10,30} in referring to it as the “conduction band” independent of its origin.
 55 The hole-like band near the X point is identified as the lower Hubbard band, following works
 56 on undoped $\text{Sr}_3\text{Ir}_2\text{O}_7$ ^{25,32}. The band maxima at Γ are commonly attributed to the $J_{\text{eff}} = \frac{3}{2}$
 57 bands^{5,25,32}, and their separation is due to the bilayer splitting present in $\text{Sr}_3\text{Ir}_2\text{O}_7$.

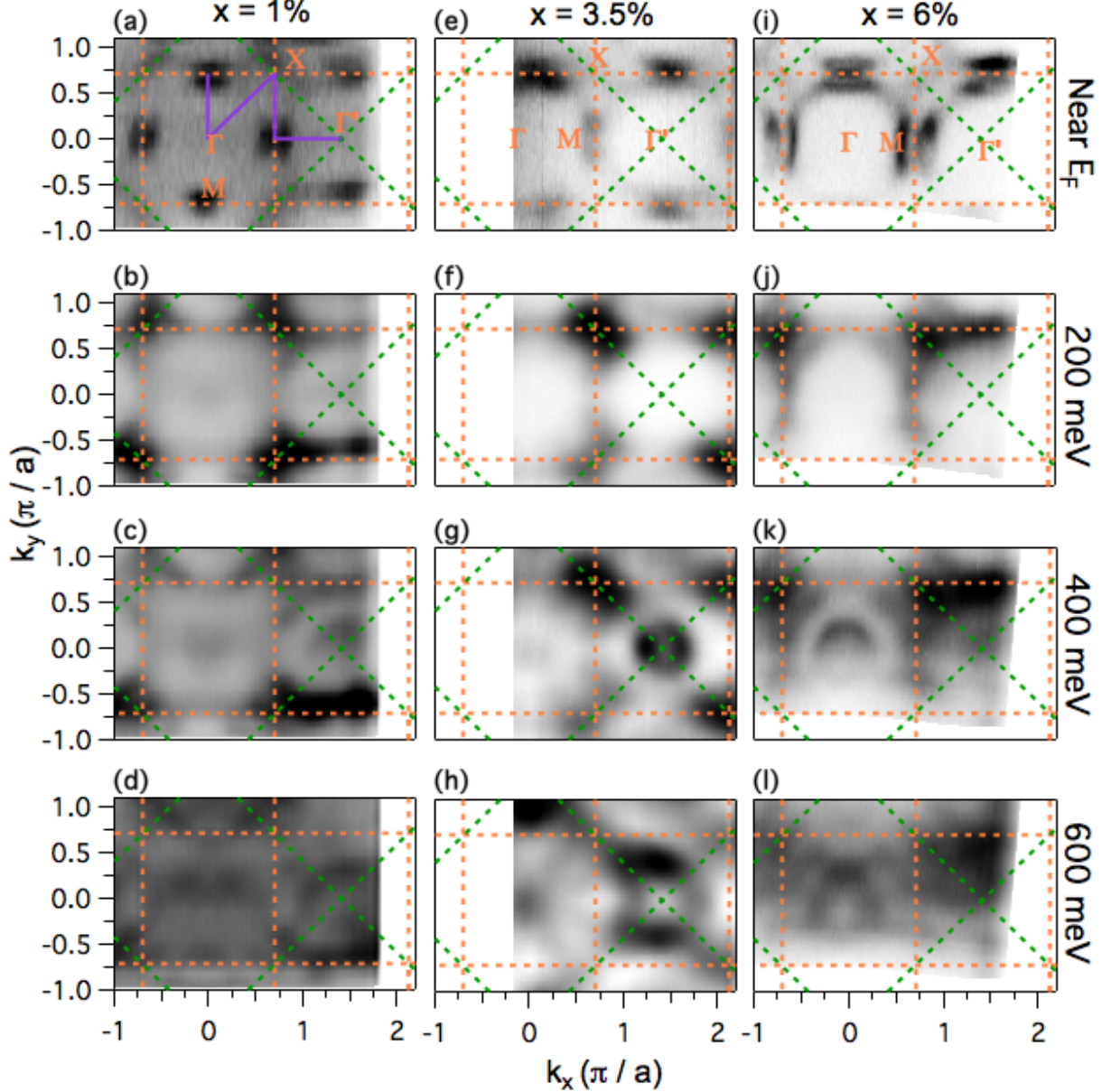


FIG. 2. Constant energy maps for $x = 1\%$ (a - d), $x = 3.5\%$ (e - h) and $x = 6\%$ (i - l) samples at binding energies from 0 to 600 meV. The orange dashed square represents the Brillouin zone of $\text{Sr}_3\text{Ir}_2\text{O}_7$ while the green dashed squares represent the Brillouin zone when the unit cell doubling due to Ir-O octahedral rotations is ignored.

58 Figure 2 shows constant energy maps of the ARPES intensity from lightly doped ($x = 1\%$)
 59 through a doping near the metal-insulator transition ($x = 3.5\%$) to heavily doped ($x = 6\%$)
 60 $(\text{Sr}_{1-x}\text{La}_x)_3\text{Ir}_2\text{O}_7$ samples. The orange dashed lines represent the boundaries of the surface
 61 Brillouin zone in the presence of either AF order or the unit cell doubling generated by the
 62 staggered rotation of Ir-O octahedra, while the green dashed lines are the boundaries of the
 63 unreduced Brillouin zone. Γ here denotes the momentum coming from normal emission of
 64 photoelectrons. Γ' is equivalent to Γ in the reduced Brillouin zone but represents a distinct
 65 crystal momentum in the larger zone. The Fermi surface for each is shown in panels (a),
 66 (e), and (i) and consists of electron-like pockets near the M point along the boundary of the
 67 reduced Brillouin zone. While these pockets are well separated in the $x = 1\%$ sample, the
 68 increased pocket size in the $x = 6\%$ sample leads to significant deviation from an elliptical
 69 shape and hybridization between adjacent pockets near the $\Gamma - X$ direction as well as along
 70 the Brillouin zone boundary. These bands are absent at a binding energy of 200 meV, shown
 71 in panels (b), (f), and (j), where the primary spectral weight arises from the $J_{\text{eff}} = \frac{1}{2}$ lower
 72 Hubbard band at the X point. At a binding energy of 400 meV, the $J_{\text{eff}} = \frac{3}{2}$ bands at Γ/Γ'
 73 are visible along with the $J_{\text{eff}} = \frac{1}{2}$ lower Hubbard band near X. At 600 meV, most bands
 74 should be of mostly $J_{\text{eff}} = \frac{3}{2}$ character, and a large number of band crossings are visible here
 75 in the constant energy maps of panels (d), (h), and (l).

76 While previous ARPES works on $\text{Sr}_3\text{Ir}_2\text{O}_7$ have primarily used the reduced Brillouin
 77 zone delineated by the orange boundaries in these figures, two features seemingly align more
 78 closely with the green zone boundaries of the unreduced Brillouin zone. The first is the
 79 difference between the spectra near the Γ and Γ' points, especially visible at a binding
 80 energy of 400 meV in the $x = 3.5\%$ sample in figure 2g (and to a lesser extent in the x
 81 $= 6\%$ sample, figure 2k). In each, a large pocket is observed at Γ' and only faint spectral
 82 weight related to a deeper band maximum is visible at Γ , though this may be related to
 83 photoemission matrix element effects at normal emission as seen in undoped $\text{Sr}_3\text{Ir}_2\text{O}_7$ ³². The
 84 second is the elongation of the lower Hubbard band pockets along the $\Gamma' - X$ direction in
 85 the $x = 1\%$ and $x = 3.5\%$ samples and, to a lesser degree along the $\Gamma - X$ direction in the x
 86 $= 6\%$ sample. In the case of the reduced (orange) Brillouin zone, these pockets should have
 87 fourfold rotational symmetry about the X point, with the same width along the $\Gamma - X$ and
 88 $\Gamma' - X$ directions, while these are not required by the unreduced (green) Brillouin zone. A
 89 similar distortion has been noted in undoped $\text{Sr}_3\text{Ir}_2\text{O}_7$ ^{20,25}, with two distinct explanations

90 that each depend on the incident photon energy. One study suggests that the bonding and
 91 antibonding bands have opposite elongations, so that the overall band structure is symmetric
 92 under the required rotation, but that a given photon energy will preferentially select one
 93 of these bands resulting in the observed elongation. The other explanation of the X point
 94 elongation comes from considering a bulk Brillouin zone in which the cross section of the
 95 first Brillouin zone at a particular k_z value is not a square. In particular, at $k_z = 0$ the point
 96 labeled Γ' here is actually the bulk Z point, and the Brillouin zone boundary is naturally
 97 elongated along $\Gamma' - X$. Most published calculations of the band structure of $\text{Sr}_3\text{Ir}_2\text{O}_7$ do
 98 not consider this three dimensional zone, and such calculations may be useful to determine
 99 the relevance of the bulk Brillouin zone for this system. We further note that there have
 100 been recent reports¹¹ showing broken symmetries in the structure of the Ir-O octahedra such
 101 that the correct lattice for $\text{Sr}_3\text{Ir}_2\text{O}_7$ is monoclinic rather than tetragonal, as the square BZ
 102 we use here would suggest. The distortions causing the system to depart from tetragonal
 103 symmetry are quite small (on the order of 0.1%), and thus should not be clearly visible in
 104 the ARPES spectra here.

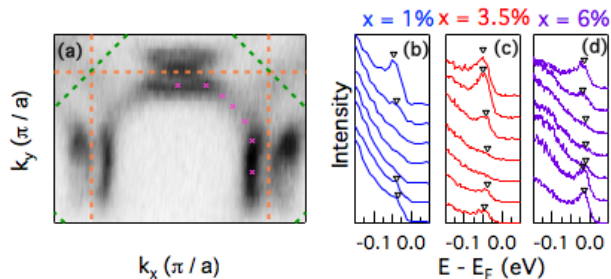


FIG. 3. Detailed evolution of M point band. (a): Fermi surface of the $x = 6\%$ sample in and near the first Brillouin zone. (b),(c),(d): EDCs taken along the arc in the $x = 6\%$ Fermi surface for the $x = 1\%$, $x = 3.5\%$, and $x = 6\%$ samples, respectively, at momentum locations marked by magenta stars in panel a. (e)-(h): Zoomed in constant energy maps of the electron-like band in the region marked by a yellow rectangle in panel a, from 10 meV above E_F to a binding energy of 40 meV near the band bottom.

105 While the primary change in the Fermi surface with increasing electron concentration is
 106 the increasing size of the nearly elliptical Fermi surface pockets in the $x = 1\%$ sample, the
 107 geometry of these pockets also changes with doping. Notably, in the $x = 6\%$ sample, whose

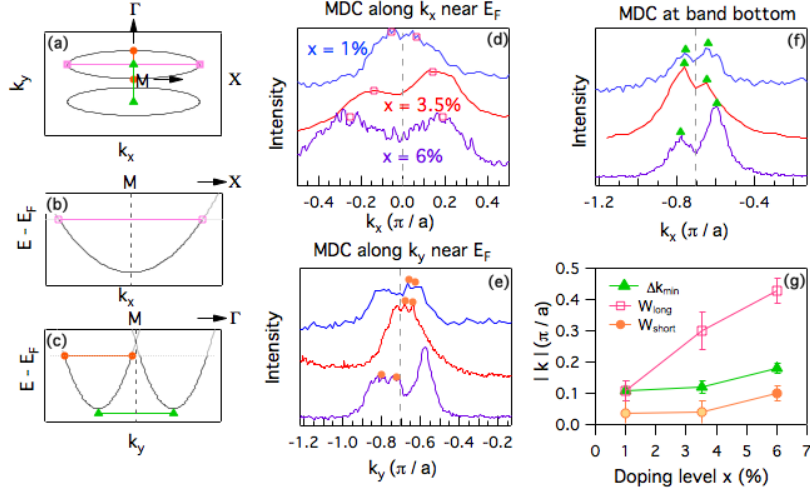


FIG. 4. Doping evolution of conduction band parameters. (a): Cartoon Fermi surface illustrating the band parameters extracted from MDCs in panels d-f. (b)-(c): Cartoon dispersions along high symmetry directions illustrating the same band parameters. (d): MDCs along the widest part of the Fermi surface pocket for each sample at E_F , with magenta squares marking k_F locations. (e): MDCs along the middle of the Fermi surface pocket in the narrower direction for each sample at E_F , with orange circles marking k_F locations. (f): MDCs along the same direction as in panel f at the binding energy of the minima of the electron-like pockets for each sample, with green triangles marking the momentum location of the band minima. (g): Doping evolution of the Fermi pocket dimensions and separation between band minima.

108 Fermi surface is replicated in figure 3a, there is spectral weight at the Fermi level in a large
 109 arc between the pockets not observed in the lower doping levels. This is reflected in the
 110 EDCs along this arc-like feature at momentum locations marked by magenta stars in figure
 111 3a shown in figure 3b-d. This arc is manifest by the small peak at E_F for the $x = 6\%$ sample
 112 for all momenta observed, and likely corresponds to dispersion of this band slightly above
 113 the chemical potential (as suggested in connection to a similar observation in³⁰). Indeed,
 114 the peak positions are at a lower binding energy nearer the $\Gamma - X$ direction. As expected,
 115 no such residual peak is observed in the EDC along the $\Gamma - X$ direction in the $x = 1\%$ and
 116 $x = 3.5\%$ samples.

117 The width of the electron pocket along its long dimension is extracted from the separation
 118 of MDC peaks taken along the k_x direction at the widest part of the pocket, as indicated
 119 for the $x = 6\%$ sample by the magenta line in figure 4a. These MDCs are shown in figure

120 4d for the $x = 1\%$, 3.5% and 6% samples. The peak locations, obtained from a fit of
 121 two Gaussian peaks and constant background, are marked by magenta squares and grow
 122 significantly farther apart with additional doping, as shown by the evolution of the magenta
 123 trace in figure 4g. The width of the pocket along the narrow direction is similarly extracted
 124 from MDCs along that direction (k_y for the pocket shown in the figure) and marked by
 125 orange circles. In each of these MDCs in figure 4e, there are three distinct peaks rather
 126 than the four that would be expected from the two nearby pockets (one from each band
 127 crossing in this direction as shown in panels a and c) due a combination of matrix element
 128 effects (like those seen in⁹, especially notable in the $x = 3.5\%$ sample where the constant
 129 energy maps only faintly show one of the two pockets) and the nearness of the two inner
 130 Fermi level crossings (especially important in the $x = 6\%$ sample). Further, these peaks
 131 are difficult to resolve above the noise level in the $x = 1\%$ and $x = 3.5\%$ samples, making
 132 the determination of the pocket width difficult. To this end, the error bars reported for
 133 this measurement in figure 4g are set by the width of the overall feature on one side of the
 134 Brillouin zone boundary and these less-certain measurements are marked by lighter circles
 135 in 4g. This width undergoes a more modest change with doping, increasing from $W_{\text{short}} =$
 136 $0.04 \pi/a$ at $x = 1\%$ to only $W_{\text{short}} = 0.09 \pi/a$ at $x = 6\%$.

137 The band minima for these electron-like bands are offset in momentum from the M
 138 point. This offset is not predicted in LDA+SOC+U calculations for the single layer Sr_2IrO_4
 139 compound and thus is likely related to the bilayer splitting in the system. This momentum
 140 offset can be measured in the separation between the two band minima along the Γ -M
 141 direction, extracted from MDC peak locations at the bottom of the conduction band. The
 142 binding energy at which these MDCs are taken is different for each doping, determined from
 143 the upturn of the EDC taken at the middle of the Fermi pocket. These MDCs are shown in
 144 figure 4f for the three dopings measured here, and the peak locations are marked with green
 145 triangles. Contrary to a rigid doping-like picture, the band minima move farther apart with
 146 increasing doping.

147 The evolution of near- E_F band dispersions in $(\text{Sr}_{1-x}\text{La}_x)_3\text{Ir}_2\text{O}_7$ can be seen in the energy-
 148 momentum spectra along high-symmetry directions shown in figure 5. The $M - \Gamma - X - M -$
 149 Γ' path for each doping is denoted by the purple line in figure 2a. Panels a, c, and e show
 150 the raw ARPES spectra, while panels b, d, and f depict the second derivative with respect to
 151 energy, commonly used to highlight band dispersions. As previously observed¹, the electron-

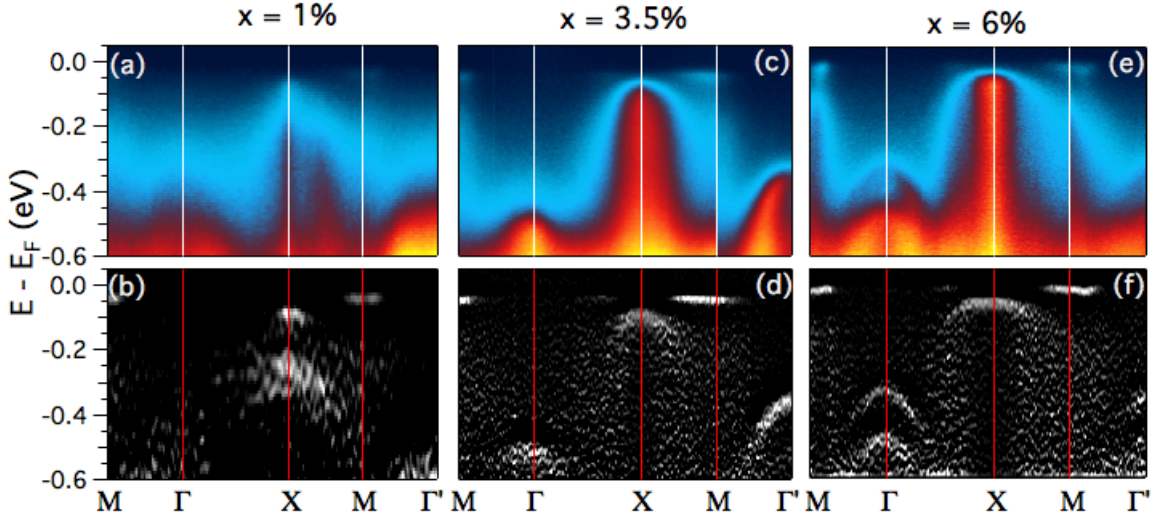


FIG. 5. Dispersion near the Fermi energy for $(\text{Sr}_{1-x}\text{La}_x)_3\text{Ir}_2\text{O}_7$ samples. (a): Raw ARPES spectrum for the $x = 1\%$ sample along a $\text{M}-\Gamma\text{-X}-\text{M}-\Gamma'$ path (marked in figure 2a). (b): Second derivative with respect to energy of (a). (c)-(f): The same as (a) and (b) for the $x = 3.5\%$ and $x = 6\%$ samples.

152 like “conduction” band becomes more filled with increasing doping and moves toward the
 153 chemical potential as the low-energy spectral weight suppression vanishes. In the $x = 1\%$
 154 sample, there are two features near the Fermi level at the X point: one at approximately
 155 300 meV, in roughly the same place as observations of the lower Hubbard band in undoped
 156 $\text{Sr}_3\text{Ir}_2\text{O}_7$ and another near 100 meV, nearer the position of the lower Hubbard band in the
 157 more heavily doped samples. In the $x = 3.5\%$ sample, there is a stronger difference in the
 158 features observed at the Γ and Γ' points than that observed in the other samples, with a
 159 band at a binding energy near 500 meV at Γ and near a shallower band near 350 meV at
 160 Γ' . While this suggests some difference between Γ and Γ' , the separation between these
 161 bands is quite close to the bilayer splitting observed at the Γ point in the $x = 6\%$ sample,
 162 suggesting a correspondence between these bands and that photoemission matrix elements
 163 likely play a role in this discrepancy. Notably, the $x = 3.5\%$ measurements were taken at
 164 a different beamline with different experimental geometry than the other measurements,
 165 which could give rise to such matrix element effects. Allowing for these matrix elements,
 166 our data support the use of the bulk Brillouin zone, in which the Γ' point is equivalent to
 167 the Z point and should be quite similar to Γ due to the minimal c-axis dispersion observed

168 in this system.

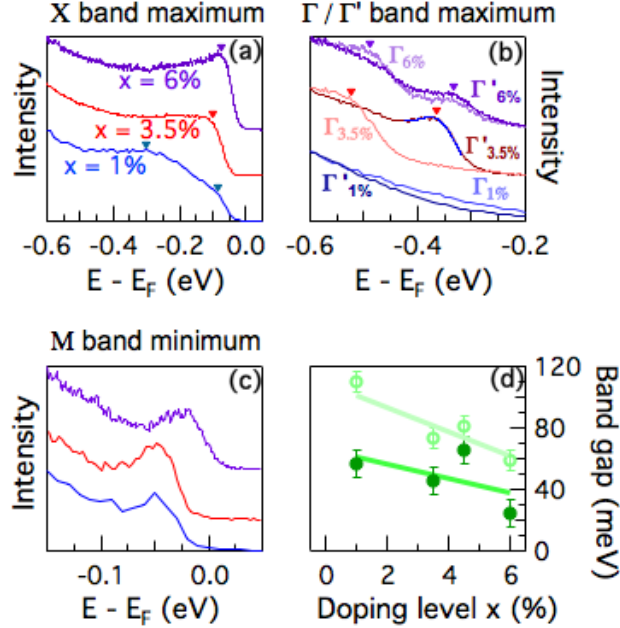


FIG. 6. Band extrema locations in $(\text{Sr}_{1-x}\text{La}_x)_3\text{Ir}_2\text{O}_7$. (a): EDCs at the X point through the maximum of the lower Hubbard band for the $x = 1\%$, $x = 3.5\%$, and $x = 6\%$ samples, with triangles marking the extracted feature locations. (b): EDCs at the Γ and Γ' points for the same samples. (c): EDCs through the band minima near the M point for the same samples. (d): Band gap extracted from the distance from the X point maximum to the M point minimum (dark circles) and from the X point maximum to E_F (light circles) as a function of doping.

169 The evolution of band separations can be more easily quantified via the analysis of en-
 170 ergy distribution curves (EDCs) as in figure 6. In panels (a) and (b), we show the EDCs
 171 corresponding to the band maxima at X and Γ/Γ' , respectively, for each doping level mea-
 172 sured here. In panel (c), we show EDCs corresponding to the momentum location of the
 173 band minimum near M, which changes slightly with doping (see discussion of figure 4). The
 174 upward movement of this band minimum near the M point with increasing doping is counter
 175 to a picture of rigid doping into an electron pocket and is due to the previously observed
 176 low-energy spectral weight suppression in the low doping regime¹. The EDCs for this near-M
 177 band are qualitatively the same for each sample, while the number of features visible in the
 178 X, Γ , and Γ' bands changes between samples.

179 From the EDCs taken at the X point in each sample (figure 6a), it appears that there

180 is a transfer of spectral weight from the 300 meV feature to the 100 meV feature with
 181 increasing doping. There are two clearly visible distinct features in the $x = 1\%$ spectrum, a
 182 flat spectrum with a leading edge near 100 meV in the $x = 3.5\%$ measurement, and a more
 183 pronounced peak near 100 meV in the $x = 6\%$ sample. The peak at higher binding energy
 184 more closely matches the lower Hubbard band position in undoped $\text{Sr}_3\text{Ir}_2\text{O}_7$, especially
 185 considering the downward shift due to the introduction of electrons. This crossover from
 186 a high-energy feature to a low-energy feature at X, which has been observed in a previous
 187 ARPES study of $(\text{Sr}_{1-x}\text{La}_x)_3\text{Ir}_2\text{O}_7$ ⁹ (though at a different doping level), may be due either
 188 to the formation of an in-gap state or due to inhomogeneity in the doping level within the
 189 measured area. STM measurements of lightly doped $(\text{Sr}_{1-x}\text{La}_x)_3\text{Ir}_2\text{O}_7$ have revealed metallic
 190 regions within tens of nanometers of regions with a density of states that is fully gapped,
 191 well within the size of the beam spot used here^{12,27}. This sample-dependent coexistence
 192 of metallic and insulating regions could explain the different doping level at which this
 193 spectral weight transfer occurs between the present study and the literature (in a previous
 194 study⁹, this crossover is observed near a doping level of $x = 4\%$). As previously discussed,
 195 the separation between the two bands at the Γ point (or the band at Γ and the band at
 196 Γ' in the case of the $x = 3.5\%$ sample) is related to the bilayer splitting in the system.
 197 Published studies of the $x = 0\%$ compound show a splitting of 180 meV between these
 198 bands^{25,32}, while the splitting in both the $x = 3.5\%$ and $x = 6\%$ samples is 158 and 157
 199 meV, respectively. The EDCs at the Γ and Γ' points in the $x = 1\%$ sample do not show
 200 clear peaks corresponding to these bands, and thus it is difficult to extract a precise value of
 201 this splitting. The difference between literature values for undoped $\text{Sr}_3\text{Ir}_2\text{O}_7$ and the doped
 202 samples here appears significant (though different handling of the spectral background in the
 203 literature may play a role), but no significant change is observed across the metal-insulator
 204 transition. Finally, the splitting between the bands at X ($J_{\text{eff}} = \frac{1}{2}$) and Γ/Γ' ($J_{\text{eff}} = \frac{3}{2}$) is \approx
 205 255 meV in the $x = 6\%$ sample and ≈ 265 meV in the $x = 3.5\%$ sample, indicating a highly
 206 similar but potentially weaker effect of spin-orbit coupling with increased doping.

207 One important doping-dependent quantity that can be extracted from the position of
 208 these bands is that of the Mott gap as a function of doping. This is related to the ambiguity in
 209 the origin of the conduction band at the M point. If this is the bottom of the upper Hubbard
 210 band, which is consistent with its momentum location in LDA+SOC+U calculations, then
 211 the Mott gap is the distance between the X point maximum and the near-M minimum. If,

212 instead, the band at M is an in-gap state, then the Mott gap is somewhat larger and can be
 213 estimated by the distance from the band maximum at X to the chemical potential. The gap
 214 values implied by the data for these two scenarios are shown in figure 6d, with dark (light)
 215 green circles marking the former (latter) explanation. Green lines provide guides to the eye
 216 for the trends of these gap values with doping. In either case, there is a net decrease in
 217 the gap magnitude over the doping range studied, with an increase across the MIT between
 218 $x = 3.5\%$ and $x = 4.5\%$. This unexpected increase is well within the error bars for the
 219 LHB - chemical potential gap, while much larger in the measured gap between the lower
 220 Hubbard band and the conduction band. This discrepancy largely comes from the vanishing
 221 of a 20 meV spectral weight suppression in the antiferromagnetic samples across the metal-
 222 insulator transition. This may indicate that the position of the lower Hubbard band is the
 223 better indicator of the Mott gap. This is in line with a previous study of $(\text{Sr}_{1-x}\text{La}_x)_3\text{Ir}_2\text{O}_7$,
 224 though our gap values are somewhat lower than those reported in that work⁹. The major
 225 part of this discrepancy is due to observation of the two bands at the X point. In that work,
 226 the lower binding energy band is not observed in samples below a doping level of $x = 5\%$.
 227 Both works agree that the gap remains open to high doping levels ($x \geq 6\%$), in contrast to
 228 the single-layer Sr_2IrO_4 where the Mott gap collapses abruptly³¹.

229 The evolution of the effective mass in the lower Hubbard band and conduction band with
 230 doping is illustrated in figure 7. Band dispersions are determined by taking EDCs at each of
 231 several momentum points along a line in the Brillouin zone, and extracting a characteristic
 232 energy for each. As the lower Hubbard band lacks a clear peak feature in the $x = 1\%$ and
 233 $x = 3.5\%$ samples, the leading edge midpoint was taken as the band position, as shown
 234 in panels (a) - (c). Similar EDC stacks for the conduction band are shown in panels (f) -
 235 (h), where a peak position can be fit. Panels (d) and (i) show these extracted dispersions
 236 for each doping level, which are then fit near the band extremum with a quadratic band
 237 in which the effective mass is a parameter. These extracted masses are plotted in panels
 238 (e) and (j) as magenta circles, normalized by the free electron mass m_0 . Error bars are
 239 derived from statistical errors in the quadratic fits, combined with the variation in mass
 240 parameter acquired from shifting the fitting range near the extremum, accounting for both
 241 the noise in band positions and asymmetry apparent in the bands. The absolute values of
 242 these band masses are similar to those reported in some systems of doped SrTiO_3 ³³. Both
 243 bands display a similar increase of a factor of 2.5 between the $x = 1\%$ and $x \approx 8\%$ samples,

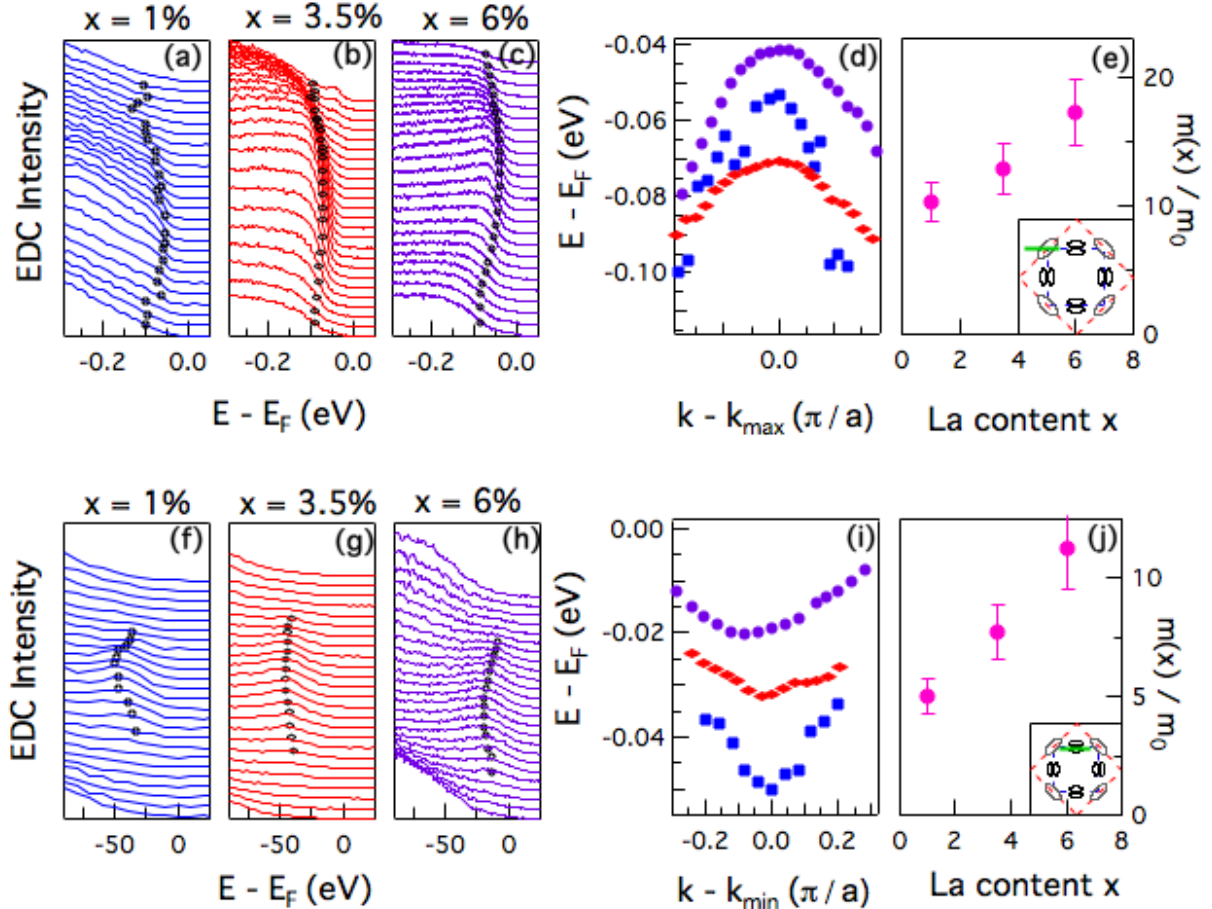


FIG. 7. Effective masses of lower Hubbard band (a), (b), (c): EDCs taken at momentum positions along the M-X direction (marked in inset to panel (e)) in the $x = 1\%$, 3.5% , and 6% samples. (d) Dispersions for the lower Hubbard band extracted from the EDC fits in (a) - (c). (e): Effective masses in $(\text{Sr}_{1-x}\text{La}_x)_3\text{Ir}_2\text{O}_7$ as a function of doping from the fits to dispersion. (f) - (j): The same as (a) - (e), for the conduction band rather than the lower Hubbard band.

244 evolving smoothly across the metal-insulator transition near $x = 4\%$. The high effective
 245 mass in metallic samples is in rough agreement with, though somewhat higher than, values
 246 from a recent work in which the mass enhancement is indirectly measured using infrared
 247 spectroscopy².

248 Figure 8 compares the doping dependent effective mass of the conduction band and lower
 249 Hubbard band of $(\text{Sr}_{1-x}\text{La}_x)_3\text{Ir}_2\text{O}_7$ with phenomena observed in cuprate superconductors,
 250 shown in figure 8a. Since the bands in the cuprates are approximately half filled, the mass
 251 renormalization is extracted from linear fits to the dispersion near the chemical potential

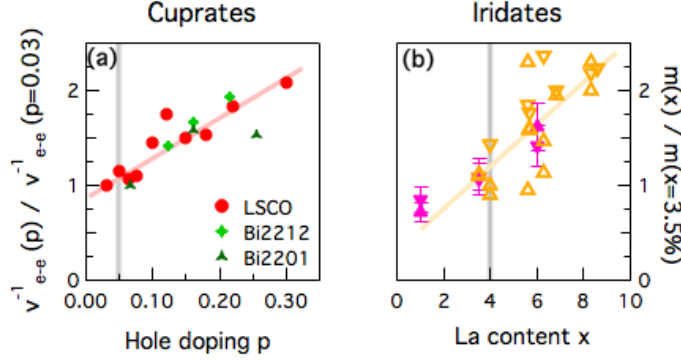


FIG. 8. Doping dependence of band renormalization in cuprates and iridates. (a): Doping dependence of band renormalization in $\text{La}_{2-x}\text{Sr}_x\text{CuO}_4$ (LSCO, red circles) $\text{Bi}_2\text{Sr}_2\text{CaCu}_2\text{O}_{8+\delta}$ (Bi2212, light green diamonds) and $\text{Bi}_2\text{Sr}_2\text{CuO}_{4+\delta}$ (Bi2201, dark green triangles) from³⁵. (b): doping dependence of effective mass in lower Hubbard band (downward pointing triangles) and conduction band (upward pointing triangles) in $(\text{Sr}_{1-x}\text{La}_x)_3\text{Ir}_2\text{O}_7$, from figures 7 and 8.

252 crossing rather than parabolic fits near band extrema as was done in $\text{Sr}_3\text{Ir}_2\text{O}_7$. Filled symbols
 253 correspond to the ratio of band velocities measured at binding energies $E_B \geq 100$ meV for
 254 three families of cuprate superconductors. This energy range is chosen to exclude explicit
 255 renormalization effects from electron-boson coupling which only impact states within an
 256 energy window of $E_b \approx \hbar\omega$ of the Fermi level. For all three cuprate families, the inverse
 257 band velocity, and thus the effective mass, increase with doping at roughly the same rate.
 258 This is in line with the observed change in effective mass in $(\text{Sr}_{1-x}\text{La}_x)_3\text{Ir}_2\text{O}_7$, suggesting a
 259 connection between the change in effective mass with doping observed in the iridates to this
 260 high-energy renormalization observed in cuprates. In cuprates, this slope change has been
 261 associated with a “high energy anomaly” wherein the band velocity drastically changes at
 262 an energy between 0.3 and 0.5 eV^{8,23}. A similar anomaly is present at high energy (near 1
 263 eV) in Sr_2IrO_4 ²¹, though no such feature has been reported in $\text{Sr}_3\text{Ir}_2\text{O}_7$. In studies with data
 264 at sufficiently high binding energy^{25,32} the ARPES spectra become broad near 1 eV, making
 265 the detailed study of dispersions at this binding energy difficult.. This type of feature is
 266 thought to be a manifestation of strong correlations, though its doping dependence does run
 267 counter to the basic picture of mass increasing with strengthening correlations^{23,26}.

268 Despite the many energy scales relevant in the ground state of $(\text{Sr}_{1-x}\text{La}_x)_3\text{Ir}_2\text{O}_7$, the pri-
 269 mary effects on the band structure with doping in the portion of the phase diagram observed

270 here can be understood in terms of electron-electron correlations. Other than the previously
271 reported spectral weight suppression at low doping, all of these changes evolve smoothly
272 across the metal-insulator transition at $x \approx 4\%$. The Mott gap weakens but does not close
273 over the observed doping range, signaling a weakening of the role of on-site Coulomb corre-
274 lations as itinerant electrons are introduced. The valence and conduction bands both show
275 an anomalous effective mass enhancement as these correlations weaken, in parallel with the
276 high-energy anomaly observed in a variety of cuprate superconductors. These similarities,
277 along with the small change in the splitting due to spin-orbit coupling and negligible effect
278 of bilayer coupling suggest that electron-electron correlations and associated Mott physics
279 are primarily responsible for the doping dependent changes in $(\text{Sr}_{1-x}\text{La}_x)_3\text{Ir}_2\text{O}_7$.

280 Acknowledgements

281 This work was primarily funded by the U.S. Department of Energy, Office of Science, Office of
282 Basic Energy Sciences, Materials Sciences and Engineering Division under Contract No. DE-
283 AC02-05-CH11231 (Quantum materials KC2202) (G.A., A.L.). Support was also provided
284 by NSF Award No. DMR 1505549 (S.D.W., T.H.).

-
- 285 ¹ Affeldt, G., Hogan, T., Smallwood, C. L., Das, T., Denlinger, J. D., Wilson, S. D., Vishwanath,
286 A., and Lanzara, A., Phys. Rev. B **95**, 235151 (2017).
- 287 ² Ahn, G., Song, S. J., Hogan, T., Wilson, S. D., and Moon, S. J., Scientific Reports **6**, 32632
288 (2016).
- 289 ³ Boseggia, S., Springell, R., Walker, H. C., Boothroyd, A. T., Prabhakaran, D., Vermeille, D.,
290 Bouchenoire, L., Collins, S. P., and McMorro, D. F., Phys. Rev. B **85**, 184432 (2012).
- 291 ⁴ Cao, Y., Wang, Q., Waugh, J. A., Reber, T. J., Li, H., Zhou, X., Parham, S., Park, S.-R.,
292 Plumb, N. C., Rotenberg, E., Bostwick, A., Denlinger, J. D., Qi, T., Hermele, M. A., Cao, G.,
293 and Dessau, D. S., Nature Communications **7** (2016).
- 294 ⁵ Carter, J.-M. and Kee, H.-Y., Phys. Rev. B **87**, 014433 (2013).
- 295 ⁶ Chikara, S., Haskel, D., Sim, J.-h., Kim, H.-s., Chen, C.-C., Fabbris, G., Veiga, L. S. I., Terzic,
296 J., Butrouna, K., Cao, G., Han, M. J., and Veenendaal, M. V., Phys. Rev. B **92**, 081114 (2015).
- 297 ⁷ Chu, H., Zhao, L., de la Torre, A., Hogan, T., Wilson, S. D., and Hsieh, D., Nat Mater **16**,
298 200 (2017).

- 299 ⁸ Graf, J., Gweon, G. H., McElroy, K., Zhou, S. Y., Jozwiak, C., Rotenberg, E., Bill, A., Sasagawa,
300 T., Eisaki, H., Uchida, S., Takagi, H., Lee, D. H., and Lanzara, A., *Phys. Rev. Lett.* **98**, 1
301 (2007).
- 302 ⁹ He, J., Hafiz, H., Mion, T. R., Hogan, T., Dhital, C., Chen, X., Lin, Q., Hashimoto, M., Lu,
303 D. H., Zhang, Y., Markiewicz, R. S., Bansil, A., Wilson, S. D., and He, R.-H., *Sci. Rep.* **5**
304 (2015).
- 305 ¹⁰ He, J., Hogan, T., Mion, T. R., Hafiz, H., He, Y., Denlinger, J. D., Mo, S.-K., Dhital, C., Chen,
306 X., Lin, Q., Zhang, Y., Hashimoto, M., Pan, H., Lu, D. H., Arita, M., Shimada, K., Markiewicz,
307 R. S., Wang, Z., Kempa, K., Naughton, M. J., Bansil, A., Wilson, S. D., and He, R.-H., *Nat*
308 *Mater* **14**, 577 (2015).
- 309 ¹¹ Hogan, T., Bjaalie, L., Zhao, L., Belvin, C., Wang, X., Walle, C. G. V. D., Hsieh, D., and
310 Wilson, S. D., *Phys. Rev. B* **134110**, 2 (2016).
- 311 ¹² Hogan, T., Yamani, Z., Walkup, D., Chen, X., Dally, R., Ward, T. Z., Hill, J., Islam, Z.,
312 Madhavan, V., and Wilson, S. D., *Phys. Rev. Lett.* **114**, 257203 (2015).
- 313 ¹³ Kim, B. J., Jin, H., Moon, S. J., Kim, J.-Y., Park, B.-G., Leem, C. S., Yu, J., Noh, T. W.,
314 Kim, C., Oh, S.-J., Park, J.-H., Durairaj, V., Cao, G., and Rotenberg, E., *Phys. Rev. Lett.*
315 **101**, 076402 (2008).
- 316 ¹⁴ Kim, J., Said, A. H., Casa, D., Upton, M. H., Gog, T., Daghofer, M., Jackeli, G., van den
317 Brink, J., Khaliullin, G., and Kim, B. J., *Phys. Rev. Lett.* **109**, 157402 (2012).
- 318 ¹⁵ Kim, J. W., Choi, Y., Kim, J., Mitchell, J. F., Jackeli, G., Daghofer, M., Van Den Brink, J.,
319 Khaliullin, G., and Kim, B. J., *Phys. Rev. Lett.* **109**, 1 (2012).
- 320 ¹⁶ Kim, Y., Sung, N., Denlinger, J., and Kim, B., *Nature Physics* **12**, 37 (2016).
- 321 ¹⁷ Kim, Y. K., Krupin, O., Denlinger, J. D., Bostwick, A., Rotenberg, E., Zhao, Q., Mitchell,
322 J. F., Allen, J. W., and Kim, B. J., *Science* **345**, 187 (2014).
- 323 ¹⁸ Korneta, O. B., Qi, T., Chikara, S., Parkin, S., De Long, L. E., Schlottmann, P., and Cao, G.,
324 *Phys. Rev. B* **82**, 115117 (2010).
- 325 ¹⁹ Li, L., Kong, P. P., Qi, T. F., Jin, C. Q., Yuan, S. J., DeLong, L. E., Schlottmann, P., and
326 Cao, G., *Phys. Rev. B* **87**, 235127 (2013).
- 327 ²⁰ Liu, C., Xu, S.-Y., Alidoust, N., Chang, T.-R., Lin, H., Dhital, C., Khadka, S., Neupane, M.,
328 Belopolski, I., Landolt, G., Jeng, H.-T., Markiewicz, R. S., Dil, J. H., Bansil, A., Wilson, S. D.,
329 and Hasan, M. Z., *Phys. Rev. B* **90**, 045127 (2014).

- 330 ²¹ Liu, Y., Yu, L., Jia, X., Zhao, J., Weng, H., Peng, Y., Chen, C., Xie, Z., Mou, D., He, J., Liu,
331 X., Feng, Y., Yi, H., Zhao, L., Liu, G., He, S., Dong, X., Zhang, J., Xu, Z., Chen, C., Cao, G.,
332 Dai, X., Fang, Z., and Zhou, X. J., *Scientific Reports* **5**, 13036 (2015).
- 333 ²² Lu, X., McNally, D. E., Moretti Sala, M., Terzic, J., Upton, M. H., Casa, D., Ingold, G., Cao,
334 G., and Schmitt, T., *Phys. Rev. Lett.* **118**, 027202 (2017).
- 335 ²³ Meevasana, W., Zhou, X. J., Sahrakorpi, S., Lee, W. S., Yang, W. L., Tanaka, K., Mannella,
336 N., Yoshida, T., Lu, D. H., Chen, Y. L., He, R. H., Lin, H., Komiya, S., Ando, Y., Zhou, F.,
337 Ti, W. X., Xiong, J. W., Zhao, Z. X., Sasagawa, T., Kakeshita, T., Fujita, K., Uchida, S.,
338 Eisaki, H., Fujimori, A., Hussain, Z., Markiewicz, R. S., Bansil, A., Nagaosa, N., Zaanen, J.,
339 Devereaux, T. P., and Shen, Z. X., *Phys. Rev. B* **75**, 1 (2007).
- 340 ²⁴ Moon, S. J., Jin, H., Kim, K. W., Choi, W. S., Lee, Y. S., Yu, J., Cao, G., Sumi, A., Funakubo,
341 H., Bernhard, C., and Noh, T. W., *Phys. Rev. Lett.* **101**, 226402 (2008).
- 342 ²⁵ Moreschini, L., Moser, S., Ebrahimi, A., Dalla Piazza, B., Kim, K. S., Boseggia, S., McMorro,
343 D. F., Rønnow, H. M., Chang, J., Prabhakaran, D., Boothroyd, A. T., Rotenberg, E., Bostwick,
344 A., and Gioni, M., *Phys. Rev. B* **89**, 201114 (2014).
- 345 ²⁶ Moritz, B., Johnston, S., and Devereaux, T., *Journal of Electron Spectroscopy and Related*
346 *Phenomena* **181**, 31 (2010).
- 347 ²⁷ Okada, Y., Walkup, D., Lin, H., Dhital, C., Chang, T.-R., Khadka, S., Zhou, W., Jeng, H.-T.,
348 Paranjape, M., Bansil, A., Wang, Z., Wilson, S. D., and Madhavan, V., *Nature materials* **12**,
349 707 (2013).
- 350 ²⁸ Qi, T. F., Korneta, O. B., Chikara, S., Ge, M., Parkin, S., De Long, L. E., Schlottmann, P.,
351 and Cao, G., *Journal of Applied Physics* **109**, 07D906 (2011).
- 352 ²⁹ Sohn, C. H., Lee, M.-C., Park, H. J., Noh, K. J., Yoo, H. K., Moon, S. J., Kim, K. W., Qi,
353 T. F., Cao, G., Cho, D.-Y., and Noh, T. W., *Phys. Rev. B* **90**, 041105 (2014).
- 354 ³⁰ de la Torre, A., Hunter, E., Subedi, A., McKeown Walker, S., Tamai, A., Kim, T., Hoesch, M.,
355 Perry, R., Georges, A., and Baumberger, F., *Phys. Rev. Lett.* **113**, 256402 (2014).
- 356 ³¹ de la Torre, A., McKeown Walker, S., Bruno, F. Y., Ricco, S., Wang, Z., Gutierrez Lezama,
357 I., Scheerer, G., Giriat, G., Jaccard, D., Berthod, C., Kim, T. K., Hoesch, M., Hunter, E. C.,
358 Perry, R. S., Tamai, A., and Baumberger, F., *Phys. Rev. Lett.* **115**, 176402 (2015).
- 359 ³² Wang, Q., Cao, Y., Waugh, J. A., Park, S. R., Qi, T. F., Korneta, O. B., Cao, G., and Dessau,
360 D. S., *Phys. Rev. B* **87**, 245109 (2013).

- 361 ³³ Wunderlich, W., Ohta, H., and Koumoto, K., *Physica B: Condensed Matter* **404**, 2202 (2009).
- 362 ³⁴ Yan, Y. J., Ren, M. Q., Xu, H. C., Xie, B. P., Tao, R., Choi, H. Y., Lee, N., Choi, Y. J., Zhang,
363 T., and Feng, D. L., *Phys. Rev. X* **5**, 041018 (2015).
- 364 ³⁵ Zhou, X. J., Yoshida, Y., Lanzara, A., Bogdanov, P. V., Kellar, S. a., Shen, K., Eisaki, H., and
365 Shen, Z.-X., *Nature* **423**, 398 (2003).
- 366 ³⁶ Zocco, D. a., Hamlin, J. J., White, B. D., Kim, B. J., Jeffries, J. R., Weir, S. T., Vohra, Y. K.,
367 Allen, J. W., and Maple, M. B., *J. Phys. Cond. Matt.* **26**, 255603 (2014).